A High-Gain Circularly Polarized Antenna Array Based on a Chiral Metastructure

Qian-Qian Li and Hai-Feng Zhang

***Abstract*— In this article, a chiral metastructure absorber (CMMA) is combined with a circularly polarized (CP) antenna array based on a sequential-phase feed network, and the differential absorption of left-handed circular polarization (LHCP) and right-handed circular polarization (RHCP) by CMMA unit is used to improve the axial ratio beamwidth (ARBW) of CP antenna array by absorbing the cross-polarization of the antenna array. The proposed CMMA unit achieves good circular dichroism at 4.9–5.2 GHz, which improves the ARBW of the antenna in this frequency band. In addition, the feed network of the antenna proposed in this article is in three-dimensional (3-D) form to reduce the coupling between the feed network and the radiation patches, so that higher gain can be obtained. The measured impedance bandwidth of the antenna is 80% (2.81–6.81 GHz), the axial ratio (AR) bandwidth is 70.8% (3.68–7.22 GHz), and the peak gain is 15.28 dBi.**

***Index Terms*— Antenna array, chiral metastructure absorber (CMMA), circularly polarized (CP), sequential-phase feed network.**

I. Introduction

NOWADAYS people's requirements for communication quality are getting higher and higher with the development of society, and antennas play an important role in communication systems as a device for transmitting and receiving electromagnetic waves [1], [2]. Microstrip antennas have been widely used in the development and improvement of antennas due to their miniaturization, lightweight, and easy integration [3]. However, the microstrip antenna still has many disadvantages such as narrow bandwidth and large loss. To solve the above problems, scholars have carried out research on microstrip antennas in terms of bandwidth expansion, gain enhancement, circularly polarized (CP), and array technology. Among them, the CP antenna is a meaningful research direction, which not only can receive electromagnetic waves of various polarizations in space but also reduce multipath interference and polarization mismatch [4], [5]. The use of a sequential-phase feed network is a better way to achieve CP, which can achieve wider bandwidth and higher gain due to the array form while realizing CP [6]. There are many design forms of sequential-phase feed networks, such as traditional impedance transformation [7], [8], [9] and t-type feed networks [10], but these methods cannot always obtain a wider bandwidth. Therefore, a feed network combining a Wilkinson power divider and a 90° phase shifter is proposed [11], [12], which can obtain a wider impedance bandwidth and axial ratio (AR) bandwidth. Such a slightly complex feed network inevitably requires a two-layer structure and this leads to severe coupling, and a three-dimensional (3-D) feed network is a good solution to this problem [13], [14], [15]. Part of the feed network being placed perpendicular to the radiation patches will greatly reduce the coupling between these two layers, which provides a good premise for high-gain antennas. However, many antennas can only achieve broadband width and high gain without considering the AR beamwidth (ARBW), which will not meet the requirements of some applications [16], [17]. Therefore, a chiral metastructure absorber (CMMA) is taken into consideration.

Electromagnetic metastructures are artificially designed periodic structures, which not only have the advantages of easy integration and lightweight but also have many exotic properties such as inverse Goos-Hanchen shift and inverse Doppler effect. Chirality means that an object cannot coincide with its mirror image by any manipulation such as rotation [18], [19]. CMMA exhibits different responses to left-handed circular polarization (LHCP) and right-handed circular polarization (RHCP), which can be divided into nonselective absorption and selective absorption [20], [21]. The difference lies in whether both polarized waves are absorbed or only one polarized wave is absorbed when LHCP and RHCP waves are irradiated on the CMMA surface. CP antennae should undoubtedly choose the latter and use the differential absorption of CMMA to the LHCP waves and RHCP waves to absorb the cross-polarization of the CP antenna to make the antenna wider ARBW. Li et al. [22] proposed a CMMA with an L-shaped folded metal wire structure, which has an absorption rate of more than 90% for LHCP waves and less than 10% for RHCP waves and it has good circular dichroism. However, it can only achieve differential absorption at a single frequency point and the through-hole design increases the difficulty of processing.

In summary, this article proposes a high-gain antenna that utilizes a CMMA frame to improve the CP antenna array ARBW. The antenna is divided into two parts, the inner part is a CP antenna array and the outer part is a CMMA frame. The CMMA unit designed to improve the antenna ARBW is an asymmetric chiral structure, which can exhibit excellent

Manuscript received 27 October 2022; revised 28 December 2022; accepted 4 January 2023. Date of publication 6 February 2023; date of current version 7 April 2023. *(Corresponding author: Hai-Feng Zhang.)*

The authors are with the College of Electronic and Optical Engineering and the College of Flexible Electronics (Future Technology), Nanjing University of Posts and Telecommunications, Nanjing 210023, China (e-mail: hanlor@163.com).

This article has supplementary material provided by the authors and color versions of one or more figures available at https://doi.org/10.1109/TAP.2023.3241379.

Digital Object Identifier 10.1109/TAP.2023.3241379

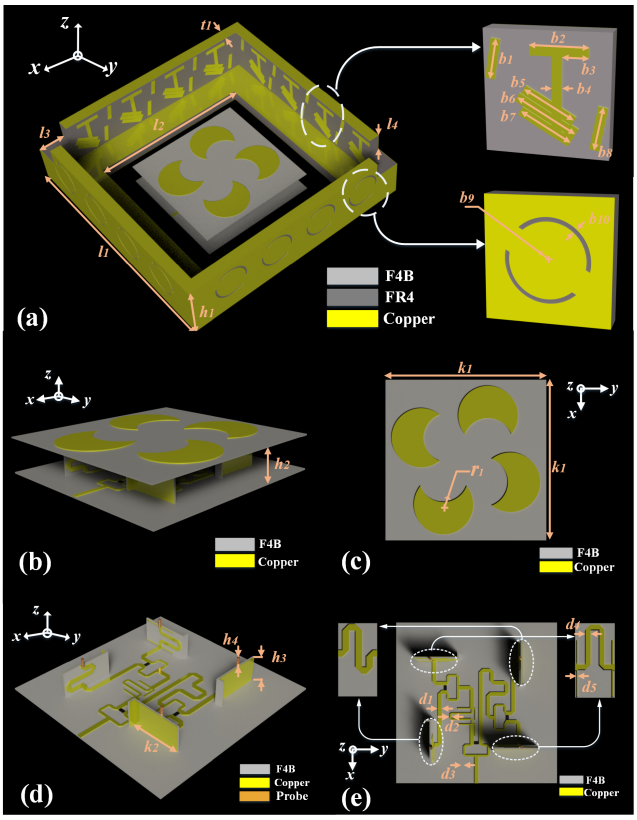

Fig. 1. Structure diagram of the antenna based on CMMA. (a) Schematic view. (b) Antenna array. (c) Top view of the antenna array. (d) Feed network. (e) Top view of the feed network ($t_1 = 6$ mm, $l_1 = 131$ mm, $l_2 = 88$ mm, $l_3 = 14$ mm, $l_4 = 10$ mm, $d_1 = 1.5$ mm, $d_2 = 0.66$ mm, $d_3 = 0.84$ mm, $d_4 = 1.1$ mm, $d_5 = 0.2$ mm, $k_1 = 65$ mm, $k_2 = 17$ mm, $h_1 = 33$ mm, $h_2 = 11.5$ mm, $h_3 = 9$ mm, $h_4 = 2.5$ mm, $r_1 = 12$ mm, $b_1 = 9$ mm, $b_2 = 12.77$ mm, $b_3 = 5.65$ mm, $b_4 = 2.2$ mm, $b_5 = 13$ mm, $b_6 = 15.1$ mm, $b_7 = 12.95$ mm, $b_8 = 10$ mm, $b_9 = 9.5$ mm, $b_{10} = 1$ mm).

circular dichroism in the range of 4.9–5.2 GHz. Antenna arrays can use this structure to achieve different absorption rates for LHCP and RHCP in this frequency range to suppress cross-polarized waves, which enables ARBW to improve by up to 50° and 24° on the *xoz* and *yoz* planes, respectively. The metal on the back of the CMMA structure can be used instead of the metal frame to enhance the reflection and thus increase the antenna gain. In addition, the sequential-phase feed network adopts a 3-D structure to reduce the coupling between it and the upper radiation patches to obtain high gain. The measured impedance bandwidth of the antenna is 80% (2.81–6.81 GHz), the AR bandwidth is 70.8% (3.68–7.22 GHz) and the peak gain is 15.28 dBi.

II. Antenna Array Design

A. Configuration of CP Antenna Array

The proposed antenna consists of two parts where the inner part is a CP antenna array printed on the F4B ($\varepsilon_r = 2.2$, tan $\delta = 0.001$) [9] substrate and the outer part is a CMMA frame printed on the FR4 ($\varepsilon_r = 4.3$, tan$\delta = 0.025$) [20] substrate, as shown in Fig. 1(a).

Fig. 1(b) and (c) are a front view and a top view of the CP antenna array, respectively. The antenna array is a double-layer structure, and the sequential-phase feed network on the

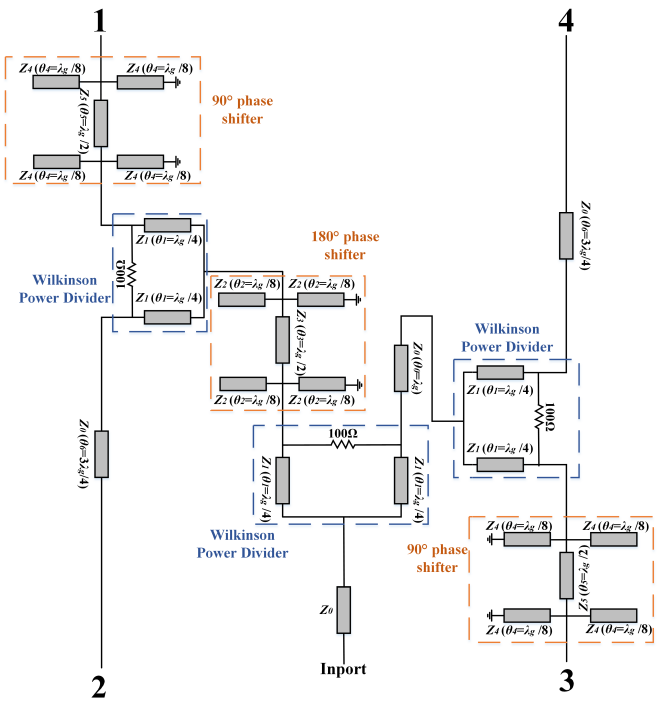

Fig. 2. Equivalent circuit diagram of the feed network.

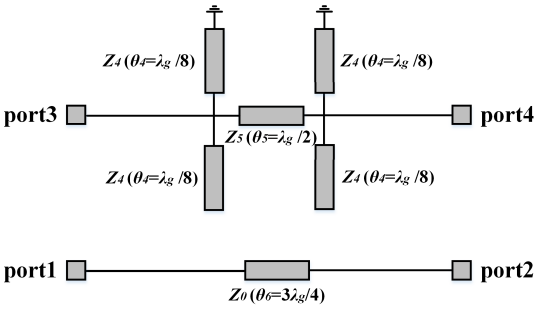

Fig. 3. Equivalent circuit diagram of the 90° phase shifter.

lower layer feeds the crescent-shaped radiation patches on the upper layer through four metal probes. Fig. 1(d) and (e) are schematic diagrams of the feed network, which use a power divider and phase shifter to make the input signal into two signals with equal amplitude and 90° phase difference. The equivalent circuit diagram of the proposed feed network is shown in Fig. 2, where the microstrip line impedance $Z_1 = \sqrt{2}Z_0 = 70.6\ \Omega$ ($Z_0 = 50\ \Omega$) of $\lambda_g/4$ (λ_g is the effective wavelength) of the Wilkinson power divider. The equivalent circuit diagram of a 90° phase shifter with a pair of short-circuit branches and a pair of open-circuit branches is shown in Fig. 3, and we perform an analysis based on the even/odd mode and superposition principle to verify its broadband phase stability

$$S_{11} = S_{22} \tag{1}$$

$$S_{33} = S_{44} = \frac{1}{2}\left(\frac{1 - jW_1}{1 + jW_1} + \frac{1 + jW_2}{1 - jW_2}\right) \tag{2}$$

$$\Delta\phi(f) = -\theta(f) + \pi - \tan^{-1}\left(\frac{1 + W_1(f)W_2(f)}{W_1(f) - W_2(f)}\right) \tag{3}$$

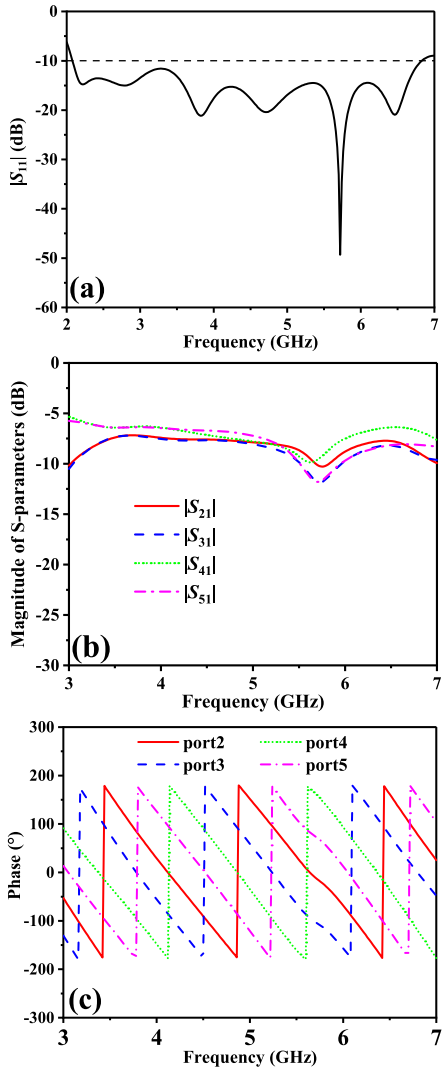

Fig. 4. Simulation results of the sequential-phase feed network. (a) $|S_{11}|$. (b) $|S_{ij}|$. (c) Phase difference of each port.

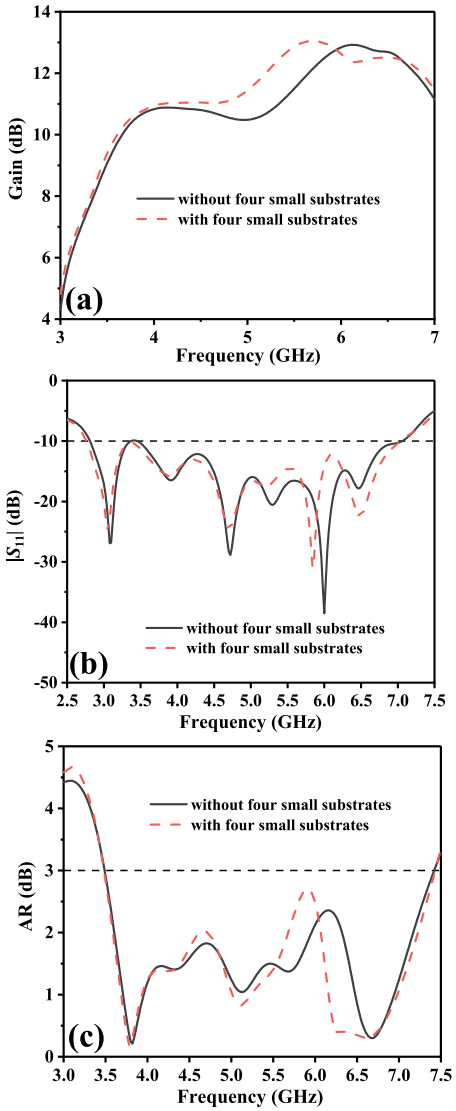

Fig. 5. Comparison of simulation results with and without four small substrates. (a) Gain. (b) $|S_{11}|$. (c) AR.

where $W_j = \overline{Y_5}(\tan(\theta_5/2))^{(-1)^{j+1}} + (-1)^j \overline{Y_4} 2\cot 2\theta_4$, $j = 1, 2$ with $\theta_5 = \pi \cdot \bar{f}$, $\theta_4 = (\pi/4) \cdot \bar{f}$. $\overline{Y_4}$ and $\overline{Y_5}$ are the normalized characteristic admittance, f_0 and $\bar{f}$ are the center frequency and normalized frequency, respectively. Then $Z_4 = 2.51Z_0$ and $Z_5 = 1.24Z_0$ can be obtained by calculation. In addition, the analysis method of the 180° phase shifter is the same as that of the 90° phase shifter except that $\Delta\varphi = 90° \pm 2°$ should be replaced by $\Delta\varphi = 180° \pm 2°$, and then $Z_2 = 1.26Z_0$ and $Z_3 = 1.62Z_0$ can be obtained by calculation.

Fig. 4(a) shows the $|S_{11}|$ of the feed network, it shows that the impedance bandwidth is 95.2% (2.08–6.84 GHz). Fig. 4(b) is the S-parameters of the feed network, the amplitudes of the four ports are relatively stable in the range of 3.5–7 GHz. Fig. 4(c) shows the phase simulation results of the feed network. The phase difference between the four output ports is relatively stable in the range of 3–7 GHz and the phase difference between them is basically kept at about 90° to ensure the generation of CP.

As shown in Fig. 1(d), the microstrip lines near the four output ports of the feed network are, respectively, printed on four other small substrates so that the entire sequential-phase feed network forms a 3-D structure. Its purpose is to reduce the mutual coupling between the radiation patches on the upper layer and the microstrip line on the lower layer to increase the gain of the antenna. In addition, four additional small substrates are added on both sides of the four vertical substrates with the feed network to enhance the reflection effect to make the whole structure more symmetrical improve the gain and make the gain curve flatter. Fig. 5(a) shows that although the gain peak is not improved much after adding four small reflective substrates, the gain is greatly improved at 5–6 GHz and the maximum can be increased by about 1.4 dBi at 5.3 GHz, which makes the whole gain curve flatter than before. Fig. 5(b) and (c) show the simulation results of $|S_{11}|$ and AR with and without four small substrates, respectively, and it can be seen that with and without four small substrates have little effect on $|S_{11}|$ and AR.

Since the distance between the upper and lower layers in the double-layer antenna has a relatively large influence on the gain of the antenna, the height of the probe connecting the

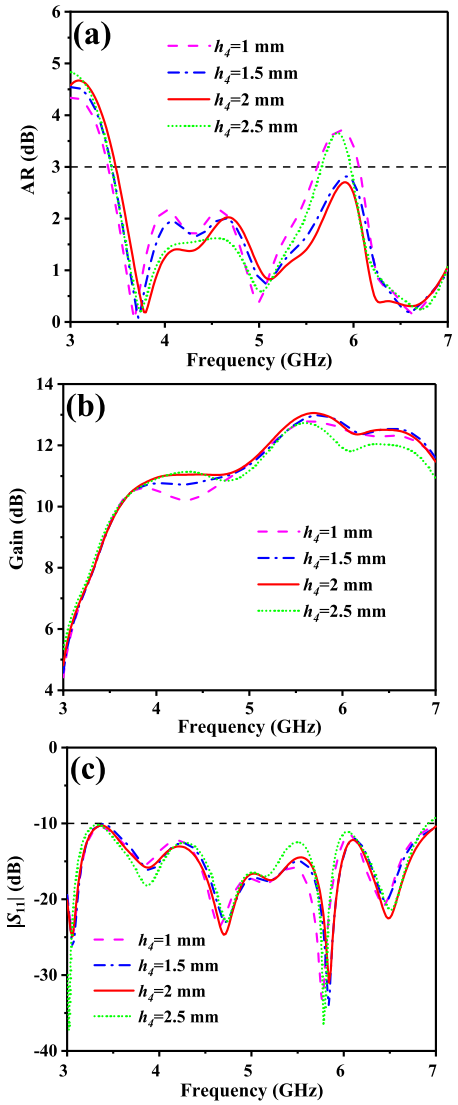

Fig. 6. Simulation results for different h_4. (a) AR. (b) Gain. (c) $|S_{11}|$.

upper and lower substrates is discussed in this article. It can be seen from Fig. 6(a) that AR will exceed 3 dB at 5.9 GHz due to a mismatch when $h_4 = 1$ mm and $h_4 = 2.5$ mm, so the spacing between the two layers should not be too large or too small. When $h_4 = 1.5$ mm and $h_4 = 2$ mm, the simulation results of AR are similar and meet the requirements. The gain curves for different h_4 are shown in Fig. 6(b). It can be seen that the peak gain is the highest when $h_4 = 2$ mm, which can reach 13.05 dBi at 5.7 GHz. Fig. 6(c) shows the simulation result of $|S_{11}|$, and it can be seen that the height of the probe almost does not affect the impedance bandwidth.

Since the phase rotation of the antenna can be determined by analyzing the electric field vector, Fig. 7 is the current distribution of the antenna at 0°, 90°, 180°, and 270°. It is obvious that the components of the current are orthogonal to each other and form a CP, and the antenna is RHCP because the rotation direction is counterclockwise.

B. Configuration of CMMA

Because the gain of the proposed antenna is not high enough and ARBW is not wide enough, the chiral metastructure is

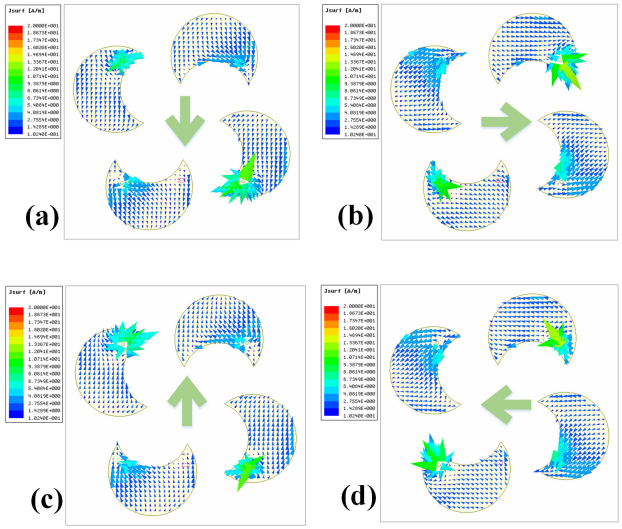

Fig. 7. Current distribution at 5 GHz. (a) 0°. (b) 90°. (c) 180°. (d) 270°.

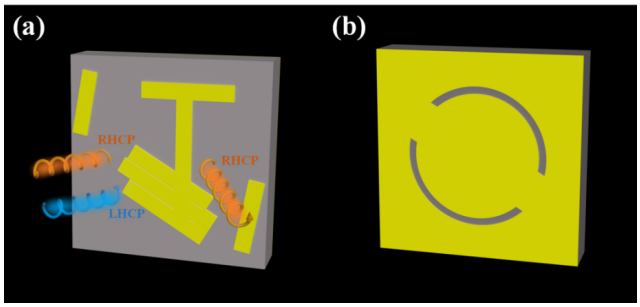

Fig. 8. Schematic of the CMMA. (a) Top view. (b) Bottom view.

combined with it in this article. This periodic arrangement of chiral metastructure has excellent circular dichroism and is called CMMA. Fig. 8 shows the configuration of the CMMA with a resonator on the upper layer, an FR4 dielectric substrate in the middle, and a metal plate with grooves on the back. The size of the CMMA unit is 28 × 28 mm^2.

The absorptivity $A(\omega)$ depends on the reflectance $R(\omega)$ and the transmittance $T(\omega)$ of the incident light incident on the metastructure, and its expression is

$$A(\omega) = 1 - R(\omega) - T(\omega) \tag{4}$$

where reflectance $R(\omega) = |S_{11}|^2$, transmittance $T(\omega) = |S_{21}|^2$. The reflection coefficient (transmission coefficient) can be expressed as $R_{ij}(T_{ij})$, where i and j represent the polarization state of the reverse (transmission) wave and the polarization state of the incident wave, respectively, and can be expressed as RHCP(+) and LHCP(−). For instance, R_{-+} and R_{+-} represent the reflection of the LHCP when the RHCP is incident and the reflection of the RHCP when the LHCP is incident, respectively. R_{--} and R_{++} represent the reflection of the LHCP when the LHCP is incident and the reflection of the RHCP when the RHCP is incident, respectively.

So the formula for absorption rate can be expressed as

$$A_- = 1 - R_{+-} - R_{--} - T_{--} - T_{+-} \tag{5}$$

$$A_+ = 1 - R_{-+} - R_{++} - T_{++} - T_{-+} \tag{6}$$

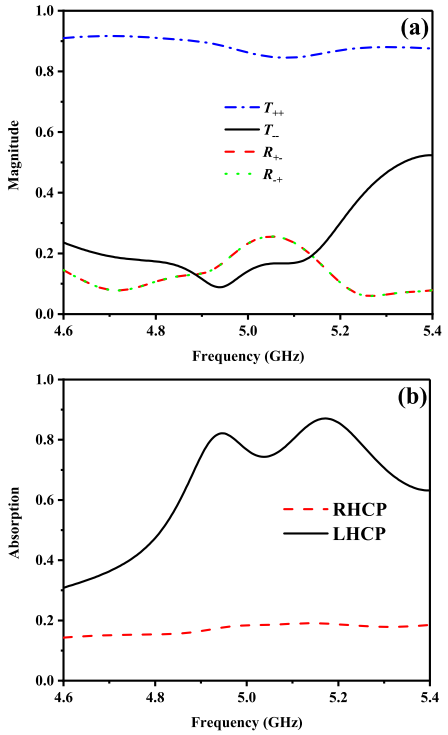

Fig. 9. (a) Simulated reflectivity and transmittance. (b) Simulated absorption rates for RHCP and LHCP.

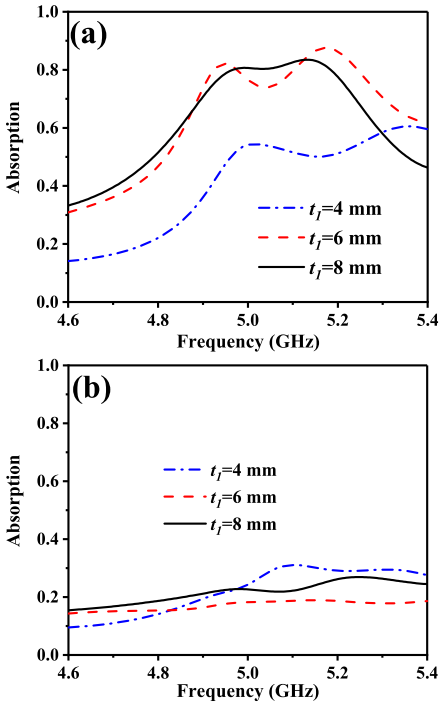

Fig. 10. Absorptivity for different t_1. (a) LHCP. (b) RHCP.

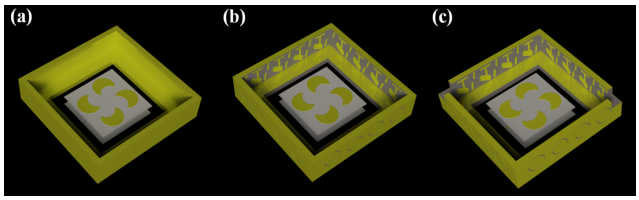

Fig. 11. Evolution diagram of the frame of the proposed antenna. (a) Metal frame. (b) CMMA frame without truncated corners. (c) CMMA frame with truncated corners.

where A_+ and A_- represent the absorptivity of RHCP and LHCP, respectively.

The CMMA proposed in this article adopts a chiral structure and its lower part consists of three branches with different lengths rotated by 60°, which can form a broadband absorption effect when the resonant frequencies of the three branches are close enough. The lengths of b_1 and b_6 on the left and right sides are 9 and 10 mm, respectively, and the rotation angles are $-10°$ and 10°, respectively. The annular groove on the back of the structure is also rotated by 30°, which further enhances the chirality of this CMMA and improves its circular dichroism. Fig. 9(a) shows the results of the transmission and reflection of this CMMA. It can be seen that the curves of the cross-polarized reflections R_{+-} and R_{-+} are the same because the impedances of the RHCP and LHCP illuminations are the same. The transmission curves T_{++} and T_{--} are significantly different and $\Delta T = T_{++} - T_{--} > 0.67$ in the range of 4.9–5.2 GHz, it can be seen that differential transmission can achieve a strong effect in a wider frequency band. Fig. 9(b) is the absorption curve calculated by (5). The absorption rate of the LHCP (cross-polarization of the antenna) wave can reach more than 75% in the range of 4.9–5.2 GHz while the absorption rate of the RHCP (co-polarization of the antenna) wave is lower than 20%. Additional information for obtaining a wider bandwidth can be found in the Supplementary Material.

The loss of the FR4 dielectric substrate in this CMMA is one of the important reasons for LHCP absorption because it is closely related to amplitude and phase matching. Therefore, the absorption rate under different substrate thicknesses t_1 is simulated in this article. As shown in Fig. 10, the absorption rate of LHCP is greatly reduced when t_1 is reduced to 4 mm and the absorptivity of RHCP is also slightly increased. At this time, the maximum absorption rate of LHCP is only 50% and the absorption rate of RHCP has reached 30%, and the differential absorption effect of the two polarizations is poor. Although there is good circular dichroism in the 4.9–5.2 GHz range as t_1 increases to 8 mm, it is still slightly lower than the result when $t_1 = 6$ mm.

C. Configuration of High-Gain CP Antenna Array

A metal frame is placed outside the proposed CP antenna array to improve its gain, as shown in Fig. 11(a). The size of the outer frame is $131 \times 131 \times 31$ mm^3, and a groove of $88 \times 88 \times 6$ mm^3 is dug in the bottom. Fig. 12(b) shows that the gain of the proposed antenna is greatly improved after the metal frame is added and the peak gain is increased by about 3–16.05 dBi. From Fig. 12(a), it can be seen that the AR bandwidth also has a slight improvement of about 0.2 GHz. The addition of the metal frame has little effect on $|S_{11}|$, as shown in Fig. 12. However, only the gain is improved is not the optimal method, so this article combines the CMMA designed above with the CP antenna array to further improve the ARBW under the premise of increasing the gain. As shown

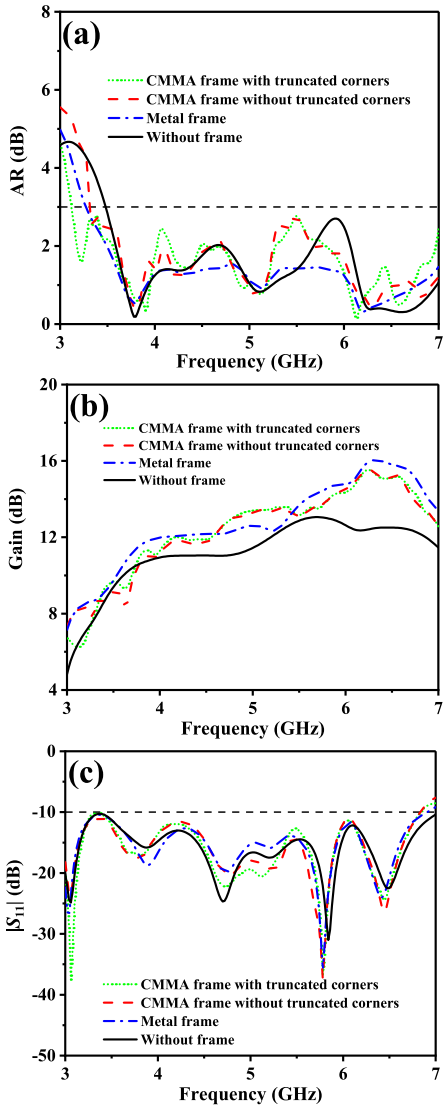

Fig. 12. Antenna with different frame and no frame comparison. (a) AR. (b) Gain. (c) $|S_{11}|$.

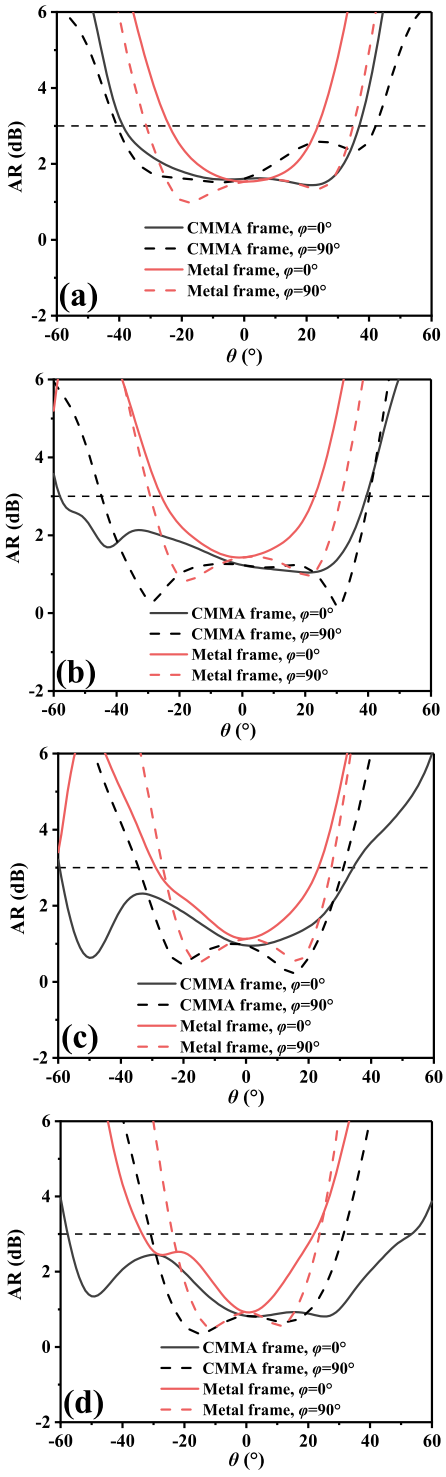

Fig. 13. ARBW simulation results using metal frame and using CMMA frame. (a) 4.8 GHz. (b) 4.9 GHz. (c) 5.0 GHz. (d) 5.1 GHz.

in Fig. 11(b), the designed CMMA cells are arranged on the outer frame in a periodical manner and four cells are arranged on each side wall of the outer frame. Fig. 12(b) shows that the peak gain when CMMA is periodically placed on the outer frame is about 15.55 dBi, which is slightly lower than that of the metal outer frame. But there is an improvement in the range of 4.6–5.4 GHz, where the maximum increase is around 1 dBi and the overall trend is not much different. This is because the metal on the back of the CMMA can replace the reflection of the metal frame, which ensures that the CMMA can also improve the ARBW of the antenna while increasing the gain. Fig. 12(a) and (c) show that the use of a CMMA frame and the use of a metal frame have little effect on AR and $|S_{11}|$.

Furthermore, the ARBW of the antenna can be effectively improved within the absorption bandwidth of the CMMA unit, which is the focus of this work. Fig. 13 shows the ARBW comparison of the CMMA frame and metal frame in the 4.8–5.1 GHz band. Fig. 13(a) shows that the ARBWs of the metal frame on the *xoz* and *yoz* planes at 4.8 GHz are 49° and 67°, respectively, while the ARBW of the CMMA frame on the *xoz* and *yoz* planes can reach 76° and 84°, respectively, which is an improvement of 27° and 17° on the *xoz* and *yoz* planes, respectively. Fig. 13(b) shows that the ARBW using the CMMA frame at 4.9 GHz is 50° and 24° higher on the *xoz* and *yoz* planes than the ARBW using the metal frame, respectively. At 5.0 GHz, the ARBW using the CMMA frame is 42° and 12° higher on the *xoz* and *yoz* planes than

TABLE I
ARBW OF ANTENNA ARRAY USING DIFFERENT FRAMES

Frequency (GHz)	Metal, *xoz* (°)	CMMA, *xoz* (°)	Improve, *xoz* (°)	Metal, *yoz* (°)	CMMA, *yoz* (°)	Improve, *yoz* (°)
4.8	49	76	27	67	84	17
4.9	49	99	50	62	86	24
5.0	53	95	42	55	67	12
5.1	56	108	52	48	63	15

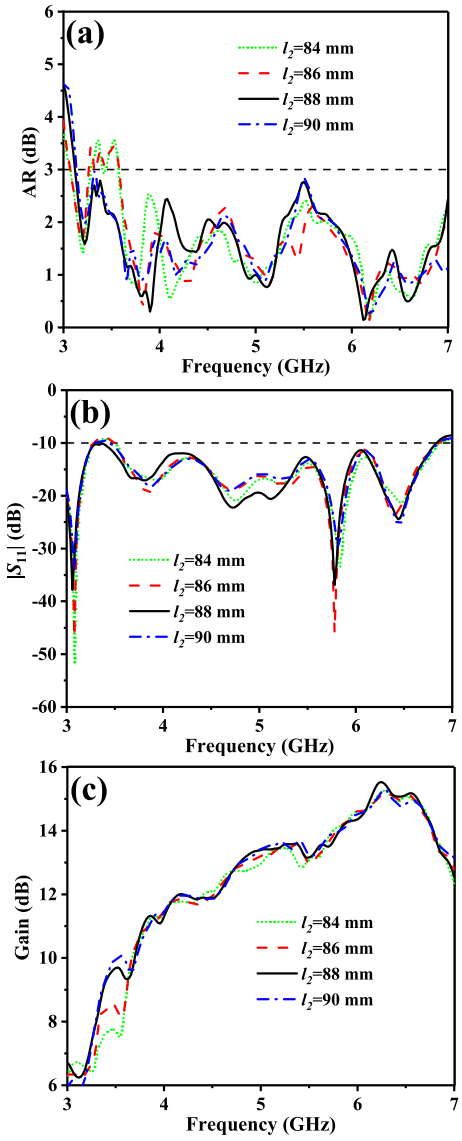

Fig. 14. Simulation results for different l_2. (a) AR. (b) $|S_{11}|$. (c) Gain.

the ARBW using the metal frame, respectively, as shown in Fig. 13(c). Fig. 13(d) shows that the ARBW using a CMMA frame at 5.1 GHz is improved by 52° and 15° in the *xoz* and *yoz* planes, respectively. The specific ARBW parameters of these four frequency points are shown in Table I. It is obvious that using a CMMA frame within 4.8–5.1 GHz can improve the ARBW on both the *xoz* and *yoz* planes than using a metal

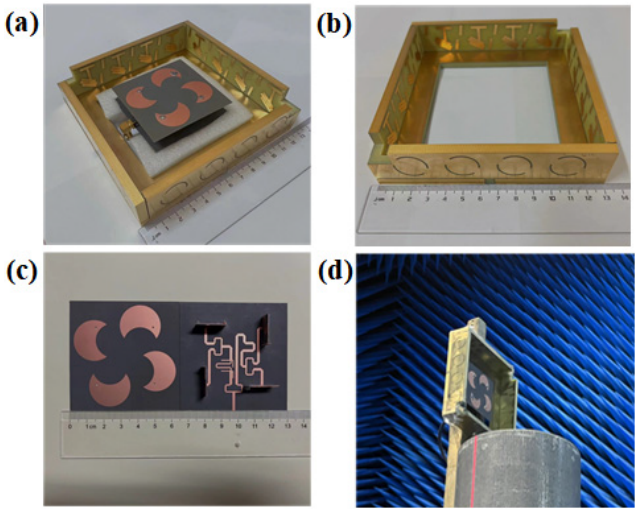

Fig. 15. Photograph of the fabricated prototype. (a) Main view. (b) CMMA frame. (c) Radiation patches and 3-D feed network. (d) Measurement of antenna array in microwave anechoic chamber.

frame, especially on the *xoz* plane. In addition, the improved frequency band of ARBW is shifted from 4.8 to 5.1 GHz to the low frequency by 0.1 GHz compared with the CMMA unit absorption band, which may be caused by the additional resonance generated by the CMMA arrangement inside the cavity. As shown in Fig. 11(c), the CMMA frame is truncated to enhance the polarization selectivity and further improve the AR. Fig. 12(a) shows that the AR bandwidth is widened by 0.2 GHz after the outer frame is truncated.

In this article, the side length l_2 of the slot at the bottom of the CMMA frame is discussed as an important parameter because it affects reflection. It can be seen from Fig. 14(a) that AR will deteriorate around 3.5 GHz when l_2 is less than 88 mm, and the AR value of this frequency point is less than 3 dB when $l_2 = 88$ mm and $l_2 = 90$ mm. It can be seen from Fig. 14(b) that the size of the slot on the back of the CMMA frame has little influence on the impedance matching, and the overall trend of S_{11} under different l_2 has little difference. It can be seen from Fig. 14(c) that when $l_2 = 88$ mm, the peak gain of this antenna is the largest and can reach 15.55 dBi. Therefore, it is most appropriate for $l_2$to be 88 mm.

III. EXPERIMENTAL VERIFICATION

In this article, the antenna array is processed and tested to verify the simulation results, and the stability is maintained using foam between the antenna and the CMMA frame, as shown in Fig. 15. The measurement results of $|S_{11}|$ are shown in Fig. 16(a) and relative impedance bandwidth is 80% (2.81–6.81 GHz) that have no too big difference with the simulation results. The test of AR was done in a Microwave Anechoic Chamber, as shown in Fig. 16(b), the measured relative AR bandwidth is 70.8% (3.68–7.22 GHz), this result is shifted to high frequency compared to the simulation, which may be the size of the dielectric plate is changed due to the extrusion deformation of the dielectric plate during the antenna welding process. It can be found from the gain measurement results of Fig. 16(c) that its overall trend is basically consistent

TABLE II
COMPARISON WITH OTHER 2 × 2 ANTENNA ARRAYS

Ref.	Frequency (GHz)	$\|S_{11}\|$ BW (%)	AR BW (%)	Peak gain (dBi)	ARBW, *xoz* (°)	ARBW, *yoz* (°)	Size of 2×2 antenna array (λ_g^3)	Polarization
[7]	6	84.74 (4.0~9.0 GHz)	57.6 (4.2~7.6 GHz)	10.04	< 45	< 45	0.9×0.9×0.053	LHCP
[8]	5.3	17.1 (4.68–5.59 GHz)	14.5 (4.81~5.58 GHz)	12	< 30	< 30	1.8×1.96×0.039	RHCP
[9]	5.8	67.8 (3.6~7.3 GHz)	49.7 (4.02~6.68 GHz)	13.1	< 60	< 60	1.6×1.6×0.154	RHCP
Proposed	5	80 (2.81~6.81 GHz)	70.8 (3.68~7.22 GHz)	15.28	108.2	103.4	1.5×1.5×0.29	RHCP

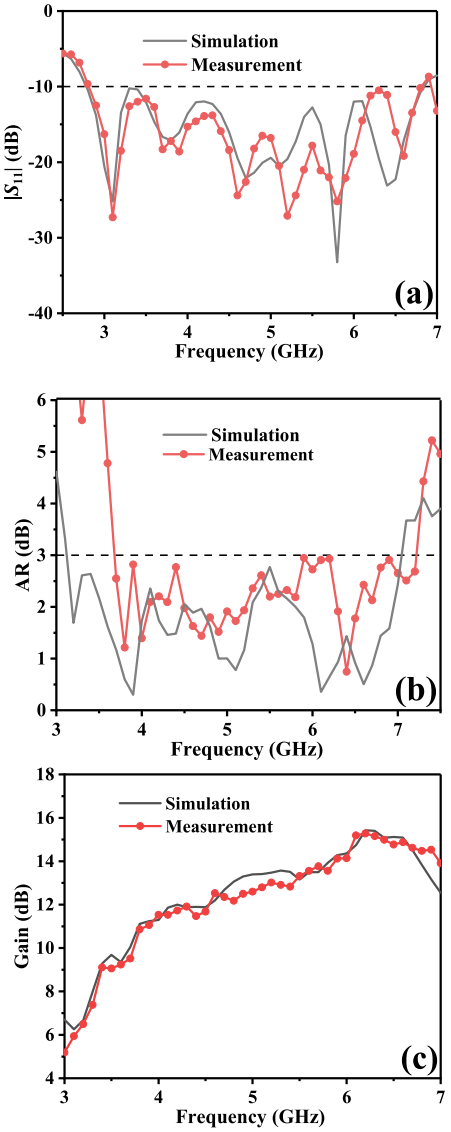

Fig. 16. Comparison of simulation results with measurement results. (a) $|S_{11}|$. (b) AR. (c) Gain.

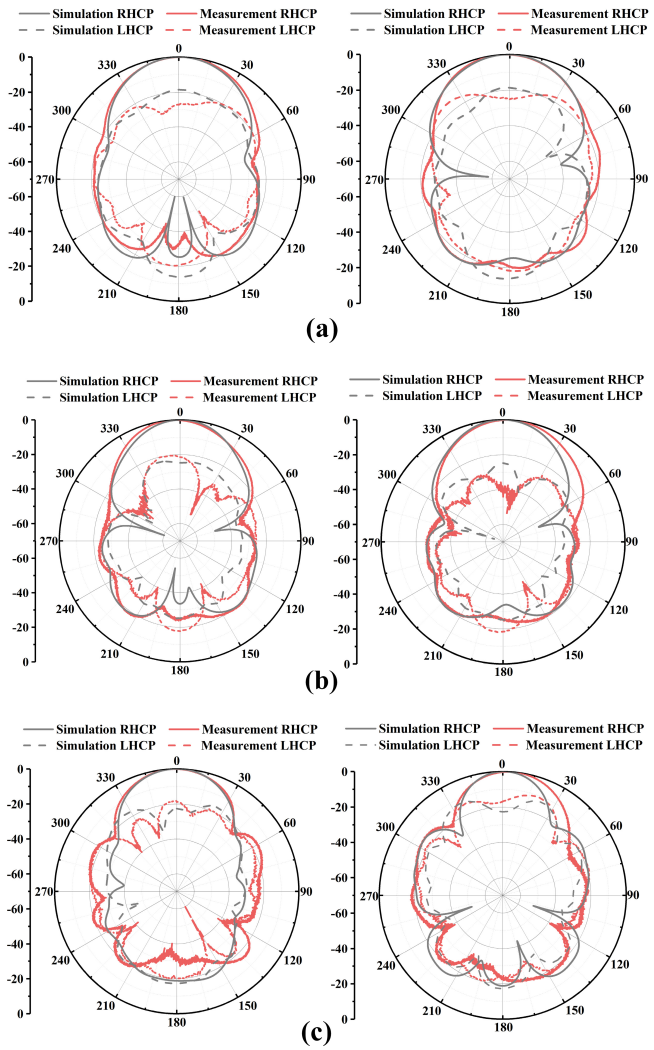

Fig. 17. Simulated and measured normalized patterns. (a) 4.5 GHz. (b) 5 GHz. (c) 6 GHz.

with the simulation results and the peak gain can reach 15.28 dBi. The slight decrease in the range of 4.5–5.5 GHz may be caused by welding errors.

Fig. 17 shows the pattern results of the measurement. The isolation of the RHCP and LHCP in the broadside direction ($\theta = 0°$) at 4.5 GHz can reach 27.3 and 25.2 dB at the *xoz* and *yoz* planes, respectively (21.2 and 40.3 dB for the two planes at 5 GHz, and 18.8 and 16.5 dB at 6.0 GHz). The ARBW measured on these two planes are 61.9° and 45.5°, respectively (108.2° and 103.4° at 5 GHz, and 56.7° and 16.5° at 6.0 GHz). The measurement results match the simulation results well and have a wide ARBW at the center frequency.

This article summarizes the index comparison of the CP antenna array proposed in this work and other reports, as shown in Table II. It can be found that the antenna has

great advantages in bandwidth and gain when the operating frequency is similar.

IV. Conclusion

A CP antenna array based on CMMA is proposed in this article. The antenna utilizes the differential absorption of LHCP and RHCP by the CMMA frame to improve the ARBW of the antenna and the metal structure on the back of the frame to enhance the reflection and increase the gain. In addition, the sequential-phase feed network adopts a 3-D form to reduce the coupling between the upper and lower layers. It is measured that the antenna can achieve an impedance bandwidth of 80% (2.81–6.81 GHz), an AR bandwidth of 70.8% (3.68–7.22 GHz), and a peak gain of 15.28 dBi. The antenna has wide bandwidth and high gain, which has broad application prospects. In addition, the proposed CMMA frame has the advantage of being detachable and is suitable for other CP antennas with the same polarization.

References

[1] W. Lin, R. W. Ziolkowski, and T. C. Baum, "28 GHz compact omnidirectional circularly polarized antenna for device-to-device communications in the future 5G systems," *IEEE Trans. Antennas Propag.*, vol. 65, no. 12, pp. 6904–6914, Dec. 2017.

[2] W. Hong, "Solving the 5G mobile antenna puzzle: Assessing future directions for the 5G mobile antenna paradigm shift," *IEEE Microw. Mag.*, vol. 18, no. 7, pp. 86–102, Nov. 2017.

[3] K. Carver and J. Mink, "Microstrip antenna technology," *IEEE Trans. Antennas Propag.*, vol. 29, no. 1, pp. 2–24, Jan. 2003.

[4] Y.-M. Cai, K. Li, Y.-Z. Yin, and W. Hu, "Broadband circularly polarized printed antenna with branched microstrip feed," *IEEE Antennas Wireless Propag. Lett.*, vol. 13, pp. 674–677, 2014.

[5] G. Feng, L. Chen, X. Xue, and X. Shi, "Broadband circularly polarized crossed-dipole antenna with a single asymmetrical cross-loop," *IEEE Antennas Wireless Propag. Lett.*, vol. 16, pp. 3184–3187, 2017.

[6] U. R. Kraft, "An experimental study on 2×2 sequential-rotation arrays with circularly polarized microstrip radiators," *IEEE Trans. Antennas Propag.*, vol. 45, no. 10, pp. 1459–1466, Oct. 1997.

[7] N. Supreeyatitikul, D. Torrungrueng, and C. Phongcharoenpanich, "Quadri-cluster broadband circularly-polarized sequentially-rotated metasurface-based antenna array for C-band satellite communications," *IEEE Access*, vol. 9, pp. 67015–67027, 2021.

[8] C. E. Santosa, J. T. S. Sumantyo, S. Gao, and K. Ito, "Broadband circularly polarized microstrip array antenna with curved-truncation and circle-slotted parasitic," *IEEE Trans. Antennas Propag.*, vol. 69, no. 9, pp. 5524–5533, Sep. 2021.

[9] Y. Cheng and Y. Dong, "Wideband circularly polarized split patch antenna loaded with suspended rods," *IEEE Antennas Wireless Propag. Lett.*, vol. 20, no. 2, pp. 229–233, Feb. 2021.

[10] J.-D. Zhang, W. Wu, and D.-G. Fang, "Dual-band and dual-circularly polarized shared-aperture array antennas with single-layer substrate," *IEEE Trans. Antennas Propag.*, vol. 64, no. 1, pp. 109–116, Jan. 2016.

[11] Z. Zhang, B. Bai, X. Li, Y. Liu, C. Sun, and Y. Zhang, "Integration of circularly polarized microstrip slot array antenna with amorphous silicon solar cells," *IEEE Antennas Wireless Propag. Lett.*, vol. 19, no. 12, pp. 2320–2323, Dec. 2020.

[12] S.-Y. Eom and H.-K. Park, "New switched-network phase shifter with broadband characteristics," *Microw. Opt. Technol. Lett.*, vol. 38, no. 4, pp. 255–257, Aug. 2003.

[13] Q. W. Lin, H. Wong, X. Y. Zhang, and H. W. Lai, "Printed meandering probe-fed circularly polarized patch antenna with wide bandwidth," *IEEE Antennas Wireless Propag. Lett.*, vol. 13, pp. 654–657, 2014.

[14] L.-L. Qiu, L. Zhu, and Y. Xu, "Wideband low-profile circularly polarized patch antenna using 90° modified Schiffman phase shifter and meandering microstrip feed," *IEEE Trans. Antennas Propag.*, vol. 68, no. 7, pp. 5680–5685, Jul. 2020.

[15] Z. Wang, S. Fang, S. Fu, and S. Jia, "An inmarsat BGAN terminal patch antenna array with unequal input impedance elements and conductor-backed ACPW series-feed network," *IEEE Trans. Antennas Propag.*, vol. 60, no. 3, pp. 1642–1647, Mar. 2012.

[16] K. L. Chung, "High-performance circularly polarized antenna array using metamaterial-line based feed network," *IEEE Trans. Antennas Propag.*, vol. 61, no. 12, pp. 6233–6237, Dec. 2013.

[17] Q. Liu, Z. N. Chen, Y. Liu, and C. Li, "Compact ultrawideband circularly polarized weakly coupled patch array antenna," *IEEE Trans. Antennas Propag.*, vol. 65, no. 4, pp. 2129–2134, Apr. 2017.

[18] T. Cao, C. Wei, L. Mao, and Y. Li, "Extrinsic 2D chirality: Giant circular conversion dichroism from a metal-dielectric-metal square array," *Sci. Rep.*, vol. 4, no. 1, pp. 1–7, Dec. 2014.

[19] L. Jing, Z. Wang, Y. Yang, B. Zheng, Y. Liu, and H. Chen, "Chiral metamirrors for broadband spin-selective absorption," *Appl. Phys. Lett.*, vol. 110, no. 23, Jun. 2017, Art. no. 221103.

[20] S. Shang, S. Yang, J. Liu, M. Shan, and H. Cao, "Metamaterial electromagnetic energy harvester with high selective harvesting for left- and right-handed circularly polarized waves," *J. Appl. Phys.*, vol. 120, no. 4, Jul. 2016, Art. no. 045106.

[21] E. Plum, "Extrinsic chirality: Tunable optically active reflectors and perfect absorbers," *Appl. Phys. Lett.*, vol. 108, no. 24, Jun. 2016, Art. no. 241905.

[22] M. Li, L. Guo, J. Dong, and H. Yang, "An ultra-thin chiral metamaterial absorber with high selectivity for LCP and RCP waves," *J. Phys. D, Appl. Phys.*, vol. 47, no. 18, Apr. 2014, Art. no. 185102.

Qian-Qian Li was born in Jiangsu, China, in 1998. She is currently pursuing the M.Sc. degree with the Nanjing University of Posts and Telecommunications, Nanjing, China.

Her main research interests include antenna array, spoof surface plasmon polariton, and chiral metastructure.

Hai-Feng Zhang was born in Jiangxi, China, in 1978. He received the M.Sc. degree in electronics science and technology from Nanchang University, Nanchang, China, in 2008, and the Ph.D. degree from the College of Electronic and Information Engineering, Nanjing University of Aeronautics and Astronautics, Nanjing, China, in 2014.

He is currently working as a Professor with the College of Electronic and Optical Engineering and the College of Flexible Electronics, Nanjing University of Posts and Telecommunications, Nanjing. His main research interests include computational electromagnetics, plasma photonic crystal, plasma stealthy, and electromagnetic properties of metamaterials.